Modelling Techniques

Lagrangian transport based on the winds of the icosahedral nonhydrostatic model (ICON)

JONAS SONNABEND[1,2,4*], JENS-UWE GROOSS[1,4], FELIX PLOEGER[1,4], LARS HOFFMANN[2,4], PATRICK JÖCKEL[3], BASTIAN KERN[3] and ROLF MÜLLER[1,4]

[1]Institute of Energy and Climate Research (IEK-7), Forschungszentrum Jülich GmbH, Jülich, Germany
[2]Jülich Supercomputing Centre (JSC), Forschungszentrum Jülich GmbH, Jülich, Germany
[3]Deutsches Zentrum für Luft- und Raumfahrt (DLR), Institut für Physik der Atmosphäre, Oberpfaffenhofen, Germany
[4]Center for Advanced Simulation and Analytics (CASA), Forschungszentrum Jülich, Jülich, Germany

Abstract

Representing atmospheric transport of constituents accurately in a chemistry climate model is a challenge. This is true in particular for a realistic representation of atmospheric transport barriers, e.g. at the edge of the polar vortices or at the tropopause. When transport is represented employing Lagrangian methods, numerical problems representing transport barriers may be obviated. Here, we present a first implementation of a Lagrangian transport model (the Chemical Lagrangian Model of the Stratosphere, CLaMS) driven by horizontal winds and vertical velocities of the icosahedral nonhydrostatic model (ICON) using the Modular Earth Submodel System (MESSy). The diabatic heating rates deduced from the temperature tendencies in the (free-running) ICON model allow vertical velocities to be determined and transport calculations in isentropic (diabatic) coordinates. The deduced diabatic heating rates agree qualitatively well with ERA5 reanalysis values in the zonal annual mean, but some discrepancies remain. Further, there is an overall agreement between the simulation and N_2O observations by the Microwave Limb Sounder (MLS) satellite instrument; in particular regarding N_2O gradients at the edge of the polar vortex. Overall, the Antarctic vortex and the associated transport barrier at its edge are well represented in the simulation, although the simulated polar vortex is larger than observed. Some differences between the observations and the Lagrangian simulation may be caused by the underlying ICON winds. The coupled ICON/MESSy-CLaMS transport scheme allows realistic simulations of tracer distributions in the free troposphere and in the stratosphere, including the representation of tracer gradients across transport barriers, a feature generally more difficult to obtain by classical Eulerian schemes.

Keywords: ICON, CLaMS, Lagrangian transport, transport barriers, N_2O, nitrous oxide, Stratosphere

1 Introduction

Chemistry climate models (CCMs) allow atmospheric dynamics, transport and chemistry to be described from the surface to the stratosphere and above. In recent years, CCMs have advanced to increasingly higher resolution and are expected to continue this advance into the future. CCMs are key tools for projections of the future development of the troposphere and the stratosphere, e.g., the future of the stratospheric ozone layer (JÖCKEL et al., 2016; DHOMSE et al., 2018). There are further applications of CCMs, including climate intervention (TILMES et al., 2021; VISIONI et al., 2023), studies of nuclear winter (MILLS et al., 2008; ROBOCK et al., 2023), assessing the impact of anthropogenic emissions and biomass burning on the atmosphere (FADNAVIS et al., 2019; ROSANKA et al., 2021), and the analysis of stratospheric transport patterns (BRINKOP and JÖCKEL, 2019;

CHARLESWORTH et al., 2020; CHARLESWORTH et al., 2023).

A CCM consists of the underlying atmospheric circulation model, a module for the calculation of transport of trace species, and modules for calculating chemical change. Further modules might, for example, simulate land use, the cryosphere and the circulation of the ocean. Relevant quantities for the atmospheric circulation like sea surface temperature (SST) and sea ice concentration (SIC) can also be prescribed and do not necessarily have to be calculated by a model.

Representing transport of atmospheric constituents in a CCM is a particular challenge because of transport barriers in the atmosphere, which separate air masses of different chemical composition. The numerical diffusion inherent in Eulerian transport schemes makes the representation of such atmospheric transport barriers difficult. The numerical diffusion caused by Eulerian transport schemes can be obviated using Lagrangian transport schemes that frequently also use diabatic vertical transport in the stratosphere (e.g., MCKENNA et al., 2002a; MCKENNA et al., 2002b; PLOEGER et al., 2010; HOPPE

*Corresponding author: Jonas Sonnabend and Rolf Müller (IEK-7), Forschungszentrum Jülich GmbH, Jülich, Germany (sonnabej@gmail.com; ro.mueller@fz-juelich.de)

et al., 2014; HOPPE et al., 2016; BRINKOP and JÖCKEL, 2019; CHARLESWORTH et al., 2020).

In earlier work (HOPPE et al., 2014) analysing long-lived tracers and age of air in the polar vortex regions in the stratosphere, it has been shown that the Lagrangian transport scheme of the Chemical Lagrangian Model of the Stratosphere (CLaMS) produces a stronger, more realistic transport barrier at the edge of the polar vortex than the classic Eulerian transport scheme of the underlying CCM (the ECHAM/MESSy Atmospheric Chemistry: EMAC JÖCKEL et al., 2006), where MESSy stands for "Modular Earth Submodel System". Differences in simulated age of air ranged up to 1 year in the Arctic polar vortex in late winter/early spring and the diabatic vertical velocities (used in the Lagrangian transport scheme) showed higher values than the EMAC vertical velocities, both in the upwelling branch in the inner tropics and in the downwelling regions in the polar vortices (HOPPE et al., 2014; HOPPE et al., 2016).

More recently, CHARLESWORTH et al. (2020) coupled the CLaMS transport to EMAC demonstrating that stratospheric transport barriers are significantly stronger for Lagrangian EMAC-CLaMS transport because of reduced numerical diffusion; in particular, stronger tracer gradients developed when using CLaMS transport around the polar vortex, at the subtropical jets, and at the edge of the tropical pipe. Furthermore, as a consequence of the decreased numerical diffusion in Lagrangian transport schemes, the moisture transport across the extratropical tropopause into the lowermost stratosphere and the water vapour mixing ratios in that region are substantially reduced, resulting in an improved comparison with satellite observations (CHARLESWORTH et al., 2023). This change in lowermost stratospheric moisture has been shown to affect the stratospheric circulation and to cause shifts in the subtropical upper-level jet streams and in the tropospheric eddy-driven jet (CHARLESWORTH et al., 2023).

Nitrous oxide (N_2O) is essentially chemically inert in the troposphere and has no significant sinks at the surface of the earth; atmospheric loss of N_2O occurs in the stratosphere through photolysis (mainly) and reaction with $O(^1D)$ (e.g. PORTMANN et al., 2012; MÜLLER, 2021). Nitrous oxide is the main source of stratospheric reactive nitrogen and thus an important driver of catalytic ozone loss cycles in the stratosphere (e.g., CRUTZEN, 1970; RAVISHANKARA et al., 2009; PORTMANN et al., 2012). Because of the property of N_2O as a tracer of air mass motion, N_2O is frequently applied for validation of model transport and transport barriers (HOPPE et al., 2014; POMMRICH et al., 2014; RUIZ and PRATHER, 2022).

The aim of this study is to provide a first assessment of the stratospheric transport using winds of the icosahedral nonhydrostatic (ICON) model. The stratospheric transport in the new model ICON has hitherto not been thoroughly analysed, a problem which is addressed through our transport simulation. In particular, we employ the CLaMS Lagrangian transport scheme

offline-driven by horizontal winds and heating rates from ICON. Comparison with measurements of N_2O of the Microwave Limb Sounder (MLS) instrument and with reanalysis data allow the performance of the coupled model to be evaluated. This study is based on the work by SONNABEND (2024), where further details are presented.

2   Description of models and data

In this paper, we present a first implementation of a Lagrangian transport model (CLaMS, see Sec. 2.2 below) driven by horizontal winds and total diabatic heating rates of the ICON model (see Sec. 2.1 below). We refer to this coupled model system as ICON/MESSy-CLaMS hereafter.

2.1   The Icosahedral Nonhydrostatic Model (ICON)

The global Icosahedral Nonhydrostatic Model (ICON) is a joint development of the German Weather Service (Deutscher Wetterdienst, DWD) and the Max-Planck-Institute for meteorology in Hamburg (ZÄNGL et al., 2015; GIORGETTA et al., 2018). ICON uses a terrain following vertical coordinate system, the smooth level vertical (SLEVE) coordinate system (LEUENBERGER et al., 2010). The SLEVE system features a hybrid pressure-altitude coordinate appropriate for application in a non-hydrostatic model (LEUENBERGER et al., 2010). The core of the horizontal ICON grid structure is a projection of a regular icosahedron onto the sphere of the earth. The horizontal resolution of ICON is easily variable (ZÄNGL et al., 2022). For the tracer transport in the standard ICON model, a mass consistent finite volume approach with fractional steps (operator splitting) is employed (REINERT, 2020; REINERT and ZÄNGL, 2021); this transport scheme was not used for the ICON/MESSy-CLaMS simulations of N_2O transport in focus here.

Here we employ the ICON version used by the DWD (numerical weather prediction model) with a model top at 80 km. The simulation is performed on a vertical grid with 90 levels of which 32 levels are entirely in the troposphere and 34 levels are entirely in the stratosphere. The ICON grid notation defines this grid as R2B4. This grid contains 20480 grid cells and has a horizontal resolution of approximately 158 km. The discretisation of the basic operators on this icosahedral grid is performed with the C-grid method (ZÄNGL et al., 2015). Here we use ICON version 2.4.

2.2   The Chemical Lagrangian Model of the Stratosphere (CLaMS)

The Chemical Lagrangian Model of the Stratosphere (CLaMS) consists of a number of different modules which have been described in detail elsewhere (e.g., MCKENNA et al., 2002a; MCKENNA et al., 2002b; KONOPKA et al., 2007; PLOEGER et al., 2010; GROOSS et al., 2014; POMMRICH et al., 2014). Briefly, CLaMS describes

Meteorol. Z. (Contrib. Atm. Sci.)
Early Access Article, 2014

J. Sonnabend et al.: Lagrangian transport in ICON

3

the state of the atmosphere by a finite number of air parcels. These air parcels are characterised by a given mixing ratio of a chemical compound. No particular value of mass is attributed to an air parcel and they are distributed on an irregular grid (MCKENNA et al., 2002a). Mixing ratios might also change chemically (MCKENNA et al., 2002b, see also below).

The air parcels are subject to physical advection by horizontal wind fields and vertical (diabatic) velocities. The motion of these air parcels is calculated with the CLaMS trajectory scheme (MCKENNA et al., 2002a), where poleward of 72° N and 72° S a polar stereographic coordinate system is used to avoid numerical problems in the polar regions. The Lagrangian scheme used here (SUTTON et al., 1994; MCKENNA et al., 2002a) employs a fourth-order Runge-Kutta scheme with a 15-min time step. The information on wind fields is needed as input for the trajectory calculation. This information can be provided from meteorological reanalyses as well as from the results of a general circulation model such as ICON (e.g., HOPPE et al., 2014; VOGEL et al., 2024; CLEMENS et al., 2024; PLOEGER et al., 2024).

CLaMS allows employing both, a detailed stratospheric chemistry scheme including heterogeneous reactions (e.g., GROOSS et al., 2014; GROOSS and MÜLLER, 2021), and a numerically more efficient simplified chemistry scheme (POMMRICH et al., 2014), which is used here.

CLaMS has been applied recently to a variety of problems ranging from polar ozone loss, stratospheric age-of-air studies, transport in the Asian monsoon anticyclone and trends in stratospheric water vapour (VOGEL et al., 2019; GROOSS and MÜLLER, 2021; POSHYVAILO-STRUBE et al., 2022; KONOPKA et al., 2022; CLEMENS et al., 2024; PLOEGER et al., 2024; VOGEL et al., 2024).

Here we focus on nitrous oxide (N_2O); the main chemical stratospheric loss processes for N_2O

$$N_2O + h\nu \rightarrow \text{prod.} \qquad (2.1)$$

$$N_2O + O(^1D) \rightarrow \text{prod.} \qquad (2.2)$$
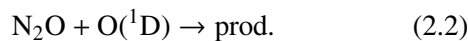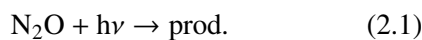
are taken into account in our simulations (see also POMMRICH et al., 2014).

By describing atmospheric transport through the calculation of trajectories, numerical diffusion can be obviated. Mixing is introduced specifically in shear zones, where strong flow deformation occurs (MCKENNA et al., 2002a; KONOPKA et al., 2005; KONOPKA et al., 2007). Thus the transport in CLaMS is particularly suited for describing the transport in the presence of transport barriers (like the tropopause, the boundary of the Asian monsoon anticyclone, or the edge of the polar vortex).

The vertical transport in the stratosphere in CLaMS is described as deviations from isentropic (potential temperature) surfaces (KONOPKA et al., 2007; PLOEGER

et al., 2010). Potential temperature is defined as

$$\theta = T \cdot \left(\frac{p_0}{p} \right)^\kappa \qquad (2.3)$$

where T is temperature, p is pressure, p_0 a reference pressure ($p_0 = 1000$ hPa) $\kappa = R/c_p$, R is the specific gas constant and c_p is the specific heat capacity at constant pressure. In this coordinate system, transport across a vertical (i.e. an isentropic) surface can take place only through diabatic heating (KASAHARA, 1974); the vertical velocity $\dot{\theta} = d\theta/dt$ is deduced from the net diabatic heating rate Q (which is commonly measured in Kelvin per second):

$$\frac{d}{d \ln \theta} = \frac{1}{\theta} \frac{d\theta}{dt} = \frac{Q}{T} \qquad . \qquad (2.4)$$

In Eq. 2.4, the net diabatic heating rate $Q = J/c_p$ where J is the diabatic heating rate per unit mass (HOPPE et al., 2016). Thus

$$\frac{d\theta}{dt} = \frac{J}{c_p} \frac{\theta}{T} \qquad . \qquad (2.5)$$

Below a reference pressure level (frequently chosen as 300 hPa; more precisely a reference level of pressure over surface pressure of 0.3), the vertical (potential temperature) coordinate in the CLaMS Lagrangian advection scheme smoothly converts to a terrain following pressure based (pressure over surface pressure) coordinate below a reference level (POMMRICH et al., 2014). Pressure, pressure tendencies ($\dot{p}$) and surface pressure are available in ICON as diagnostic variables. The use of the terrain following tropospheric CLaMS coordinate allows tropospheric vertical velocities, expressed as $\dot{p}$ to be represented in the Lagrangian transport (POMMRICH et al., 2014).

2.3 The Modular Earth Submodel System (MESSy)

The Modular Earth Submodel System (MESSy) provides a middleware which allows different numerical models of the earth system to interact (JÖCKEL et al., 2005; JOECKEL et al., 2010). Since the successful implementation of the climate model ECHAM within the MESSy framework (JÖCKEL et al., 2006; JOECKEL et al., 2010), many studies assessing the impact of anthropogenic emissions and biomass burning on the atmosphere or analysis of stratospheric transport patterns (e.g., BRINKOP and JÖCKEL, 2019; CHARLESWORTH et al., 2020; ROSANKA et al., 2021) were conducted.

The MESSy model framework is subdivided into basemodels and submodels, which are connected by the basemodel and the submodel interface layers. With the help of the interface layers and the submodels, chemical tracer transport, online diagnostic tools, and many

other models can interact with the basemodel (Joeckel et al., 2010; Jöckel et al., 2016). ICON, as an atmospheric circulation model, is implemented as a basemodel in MESSy. The MESSy version used in this study is 2.54.0.3 including ICON version 2.4.

2.4　Measurements of nitrous oxide by the Microwave Limb Sounder

The Earth Observing System (EOS) Microwave Limb Sounder (MLS, Waters et al., 2006) is an instrument onboard the EOS Aura satellite. Aura was launched on 15 July 2004 and takes measurements since August 2004 until today. The MLS scans the Earth's limb from the surface to ~95 km altitude every ~26 s, which allows atmospheric observations to be taken by MLS from 82° S to 82° N. MLS provides daily global coverage. From the microwave radiance measurement a large number of profiles of the vertical abundance of trace species are deduced (e.g., Livesey et al., 2021), here MLS measurements of N_2O are of particular importance. MLS N_2O measurements are reported as molar (or volume) mixing ratios; "ppb" means parts per billion, i.e. a molar mixing ratio of 10^{-9}. The vertical resolution of MLS N_2O measurements is 4–6 km. Ideally, one would apply the MLS averaging kernels to the simulated data for comparison. However, this is more important for specific comparisons than for climatologies of N_2O that are already subject to averaging. Furthermore, a perpetual model simulation (Sec. 3.1) can only be compared in a limited way with MLS measurements in a particular year or even with an MLS climatology.

We use MLS v4.2 data; as we focus here on seasonal to annual changes (and not on long-term variability and trends) our use of MLS N_2O will therefore not be affected by the drift detected in the v4.2 data set (Livesey et al., 2021). The best accuracy of MLS v4.2 N_2O data is achieved in the middle stratosphere (~650–800 K); the accuracy at 100 hPa (~400 K) is 124 ppb (44 %), at 68 hPa (~450 K) is 55 ppb (22 %), at 46 hPa (~500 K) 30 ppb (10 %), at 22 hPa (~650 K) 10 ppb (6 %) and at 10 hPa (~800 K) 7 ppb (7 %).

For the MLS climatologies of nitrous oxide (N_2O) the measurements were interpolated on isentropic levels for each vertical profile. The vertically interpolated profiles are binned horizontally to a regular $2° \times 2°$ longitude-latitude grid. The accumulation in bins is done for each month individually for the time period of 2005–2017 and averaged for each month.

2.5　The ERA5 reanalysis

A reanalysis combines observations into a globally complete and consistent dataset employing a model. This technique, referred to as data assimilation, is commonly used to estimate the (initial) state of the atmosphere for numerical weather prediction. A reanalysis employs a consistent (unchanged) data assimilation technique to long time series to achieve a homogeneous (as far as possible) data set. Here we use the most recent reanalysis available from the European Centre for Medium-Range Weather Forecasts (ECMWF) (ERA5, Hersbach et al., 2020) to assess the quality of wind and transport patterns simulated by the ICON/MESSy-CLaMS model. ERA5 is based on the integrated forecasting system Cy41r2. The residual circulation in the stratosphere and the structure and magnitude of radiative heating were already reasonably represented in ERA-Interim, the predecessor of ERA5 (Fueglistaler et al., 2009), but ERA5 features improved model physics, core dynamics and data assimilation compared to ERA-Interim (Hersbach et al., 2020).

3　Model design and model setup

3.1　The coupling of ICON/MESSy with CLaMS

In the present study, horizontal winds calculated on the ICON grid are interpolated onto a regular (latitude-longitude) grid using the GRid AGGregation (GRAGG) submodel (Kern and Jöckel, 2016, see also appendix 1). Vertical winds are deduced from ICON heating rates (see below Sec. 3.2 for details). For this purpose, the submodel CLaMS is adjusted so that data exchange with the basemodel ICON, and any other MESSy submodels, is possible. The data exchange is organised with the generic submodel CHANNEL. The submodel CHANNEL allows a set of prognostic and diagnostic variables of the basemodel (i.e. ICON) to be accessed. The access to these variables is at every integration time step and for all other submodels.

The time step in ICON used here is 600 s; the CLaMS transport is called after each ICON time step, the timestep is thus 600 s as well.

The ICON/MESSy-CLaMS simulation is a 10-year time slice (perpetual) simulation with dynamical and chemical boundary conditions (monthly means for 2005) repeating every year (like for a perpetual simulation). Dynamical boundary conditions constitute SSTs and SIC valid for 2005.

Boundary conditions for long-lived tracers are prescribed at the lower model boundary (i.e. at the ground). In the simulations reported here, the focus is on nitrous oxide (N_2O). For the lower boundary of N_2O ground-based baseline observations are used; the prescribed N_2O boundary is zonally symmetric but varies with the season (Pommrich et al., 2014). Like in earlier work (Pommrich et al., 2014), the photolysis rates were calculated as diurnal averages using the CLaMS photolysis code in spherical geometry (Becker et al., 2000), which is also implemented in the MESSy submodel DISSOC (Sander et al., 2019).

Furthermore, SSTs and SIC (for the year 2005) are repeating every year and are taken from the AMIP II simulations (Taylor et al., 2000); they are interpolated from the original grid structure to the ICON grid structure used here.

Meteorol. Z. (Contrib. Atm. Sci.)
Early Access Article, 2014

J. Sonnabend et al.: Lagrangian transport in ICON

5

3.2 Heating rates and vertical winds from ICON simulation

The vertical transport in CLaMS requires that heating rates are available (see Sec. 2.2). In the case of ICON, temperature tendencies dT/dt are available on surfaces of constant z (i.e. altitude or volume) from all processes that cause diabatic heating adding up to the net diabatic heating Q.

The temperature tendencies ΔT_i from all processes that cause diabatic heating are added up to the net diabatic heating Q,

$$Q = \left(\frac{dT}{dt}\right)_{radsw} + \left(\frac{dT}{dt}\right)_{radlw} + \left(\frac{dT}{dt}\right)_{turb} + \left(\frac{dT}{dt}\right)_{drag} + \left(\frac{dT}{dt}\right)_{pconv} \quad (3.1)$$

where temperature tendencies come from short- and longwave radiation (radsw and radlw), turbulence (turb), subgrid-scale and gravity wave drag (drag) and convective plumes (pconv). Equation 3.1 can be written in difference form for a time step Δt

$$Q = \left(\Delta T_{radsw} + \Delta T_{radlw} + \Delta T_{turb} + \Delta T_{drag} + \Delta T_{pconv}\right)/\Delta t \quad (3.2)$$

For an ideal gas the thermodynamic energy equation is (e.g., FUEGLISTALER et al., 2009)

$$\frac{dT}{dt} = \frac{R}{c_p}\frac{T}{p}\frac{dp}{dt} + \frac{J}{c_p} \quad (3.3)$$

here d/dt is the material derivative (KASAHARA, 1974)

$$\frac{dT}{dt} = \left(\frac{\partial T}{\partial t}\right)_z + \vec{v}\,\nabla_z T + \frac{dz}{dt}\frac{\partial T}{\partial z} \quad (3.4)$$

where z is held constant, which implies that volume is constant. Equation 3.4 is likewise valid for a general vertical coordinate s (KASAHARA, 1974). Because

$$\left(J = c_v \frac{dT}{dt}\right)_{V=const.} \quad (3.5)$$

together with equation 2.5

$$\frac{d\theta}{dt} = \frac{c_v}{c_p}\frac{\theta}{T}\left[\left(\frac{dT}{dt}\right)_{V=const.}\right]_{diabatic} \quad (3.6)$$

where the temperature tendencies $(dT/dt)_{V=const.}$ are taken from ICON (Eq. 3.1).

4 Results

4.1 Winds and transport

The horizontal winds of the ICON/MESSy simulation are integrated into the Lagrangian transport calculation
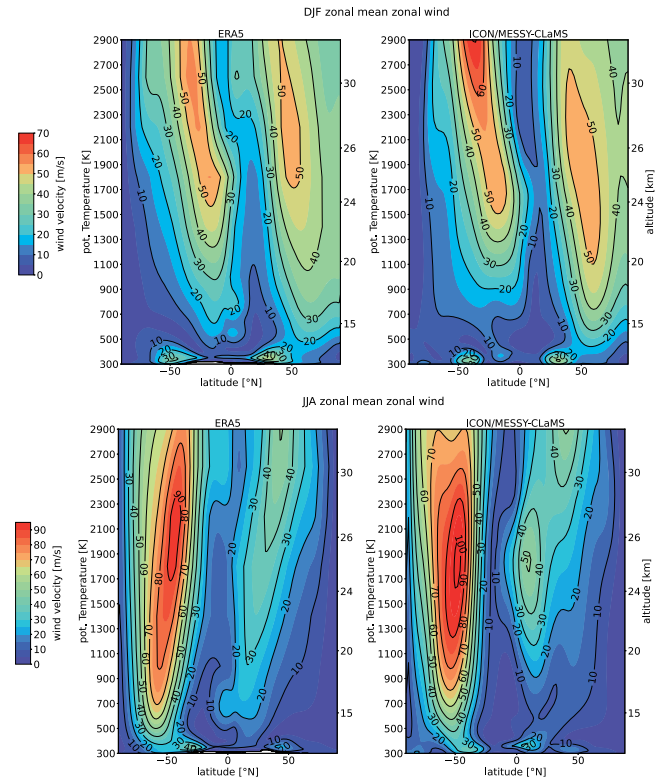

Figure 1: Zonal mean of horizontal wind speed from ERA5 2005–2014 climatology (left column) and ICON/MESSy-CLaMS ten year climatology (right column). Top: December to February (DJF); bottom: June to August (JJA).

(Sec. 3.1, see also Figure 1, right column). The stratospheric jets are clearly noticeable, in particular at the edge of the polar vortex in both, the northern and the southern hemisphere (Figure 1). A comparison with the ERA5 2005–2014 climatology shows overall good results, although the peak wind velocities are larger in ICON/MESSy-CLaMS than in ERA5 (Figure 1). Note that a very close correspondence cannot be expected as the results of the ICON/MESSy-CLaMS simulation come from a free (perpetual) run (which does not exactly represent the conditions in a particular year).

Vertical winds in the CLaMS transport scheme based on isentropic surfaces are deduced as diabatic heating rates (see Sec. 3.2). The zonal annual mean diabatic heating rates deduced from the temperature tendencies in the ICON model (Sec. 3.2) show the expected behaviour of ascent in the tropics and descent over the poles (Figure 2); there is a good qualitative agreement with the ERA5 reanalysis heating rates. However, there remain some differences between ICON and ERA5 heating rates, such as somewhat stronger heating rates in ERA5 in the lower tropical stratosphere and somewhat stronger heating rates in ICON (both in the tropics and extratropics) in the middle stratosphere at about 600–700 K (Figure 2). However, the agreement between the ICON/MESSy-CLaMS model and the ERA5 reanalysis in terms of diabatic heating rate is better than the comparison with ERA-interim (not shown).
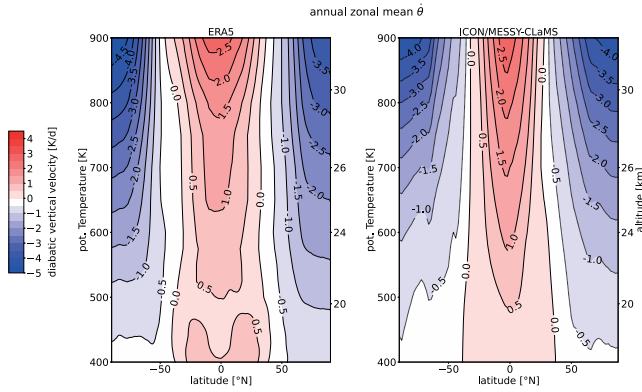
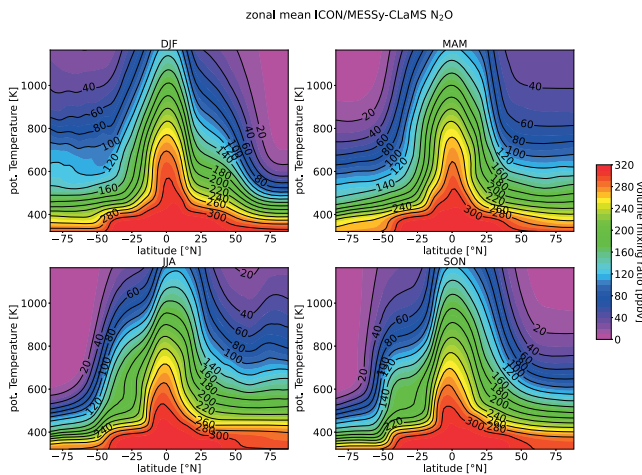**Figure 2:** Zonal annual mean diabatic heating rate, left panel ERA5, right panel from ICON/MESSy-CLaMS.

Figure 3: Zonal mean nitrous oxide (N$_2$O) mixing ratio for a seasonal ten year climatology separated in four seasons (see individual panels) simulated by ICON/MESSy-CLaMS. Vertical range from 350 K potential temperature to 1200 K.

Figure 4: Zonal mean nitrous oxide mixing ratio for winter and summer. MLS 2005–2017 climatology (left panels). Ten year ICON/MESSy-CLaMS simulation climatology (right panels). Top panels: DJF, bottom panels JJA. Vertical range from 450 K potential temperature to 900 K. (MLS averaging kernels have not been applied to the simulated N$_2$O fields.)

4.2 Simulation of nitrous oxide

Chemical tracers in CLaMS are subject to transport, mixing and chemical reactions (MCKENNA et al., 2002b; GROOSS et al., 2014; POMMRICH et al., 2014). The simulated seasonal zonal mixing ratios of nitrous oxide are shown in Figure 3. This zonal climatology is calculated as a time average of ten years of simulation for each season individually. Nitrous oxide is a long lived species (e.g., MÜLLER, 2021; RUIZ and PRATHER, 2022), which is transported upward through the tropical pipe in the stratosphere. In the course of this upward transport, N$_2$O is decomposed in the tropics in the middle stratosphere and above (PORTMANN et al., 2012). A robust peak of high mixing ratios is simulated consistently throughout the seasons. The seasonal change in the lower stratospheric region in the winter hemisphere exhibits air masses with low N$_2$O concentrations, which are transported downward by diabatic descent from the upper stratosphere.

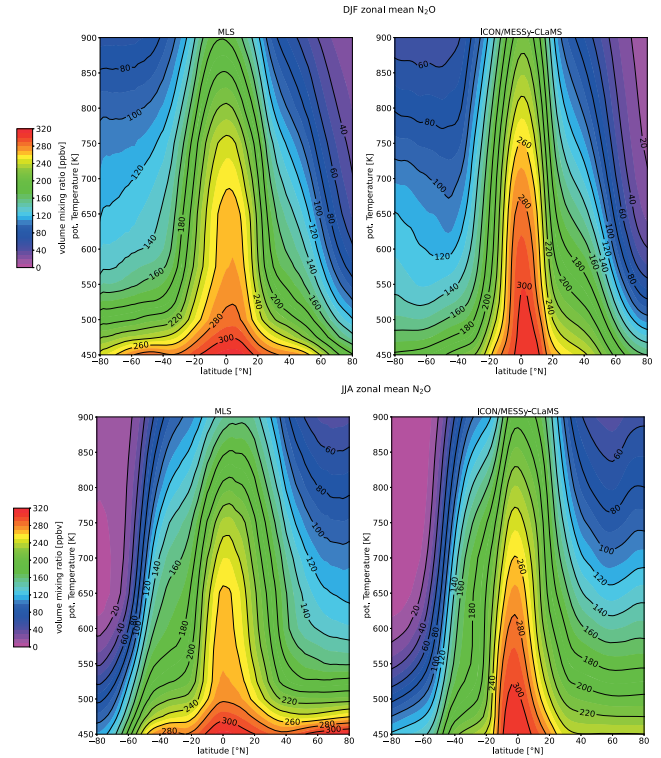A comparison of the simulated zonal mean nitrous oxide mixing ratios with MLS observations is shown in

Figure 4, for northern hemisphere winter (top) and summer (bottom). Upward transport of nitrous oxide mixing ratio in the tropical pipe and diabatic descent over the winter poles is seen in both, the simulation and the MLS observations (Figure 4). Further, the decline of nitrous oxide with altitude because of chemical loss at greater heights in the stratosphere (see Eqs. 2.1 and 2.2) is clearly visible. However, simulated nitrous oxide mixing ratios in the tropical pipe are larger than observed. Also, while the model captures high mixing ratios of nitrous oxide at lower altitudes – as expected for a tropospheric source gas – (Figure 3), the decline of N$_2$O mixing ratios in the summer hemisphere extratropics is stronger in ICON/MESSy-CLaMS than observed (Figure 4). The different simulated N$_2$O patterns agree in principle with the observed differences in upwelling between the simulation and ERA5. However, there remain some discrepancies in the magnitude of the diabatic heating rates between ICON and ERA5 (Figure 2); further, there are also uncertainties in the MLS N$_2$O measurements in the lower stratosphere (Sec. 2.4).

An isentropic cross section of nitrous oxide at 500 K (~18 km) is shown in Figure 5; left panels show MLS observations and right panels the results of the simulation (ICON/MESSy-CLaMS). The tropical band in the observations contains air with lower mixing ratios of nitrous oxide than the simulation. In the MLS observa-
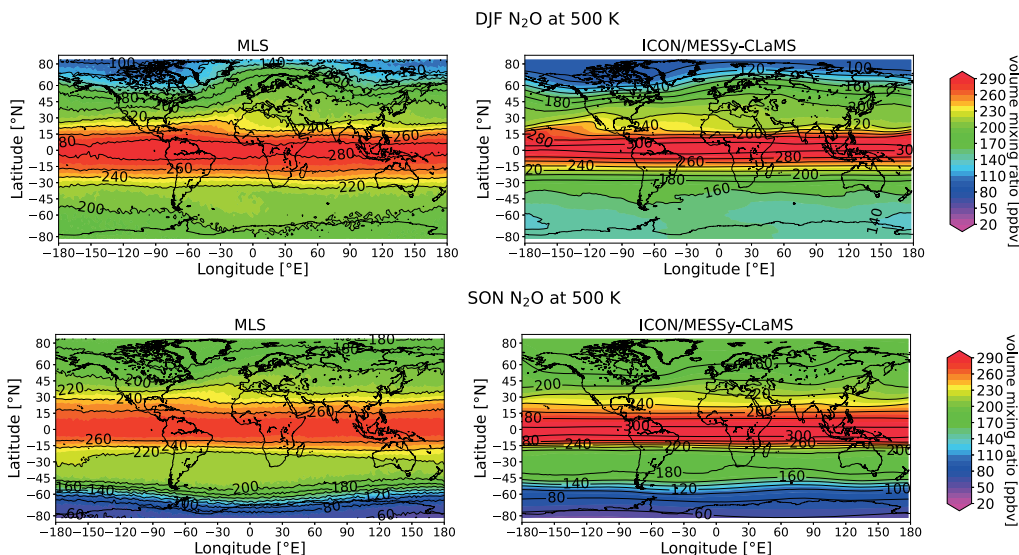
Meteorol. Z. (Contrib. Atm. Sci.)
Early Access Article, 2014

J. Sonnabend et al.: Lagrangian transport in ICON

7

Figure 5: Nitrous oxide (N_2O) mixing ratio for seasonal climatologies at 500 K (~18 km). MLS 2005–2017 climatology (left panels). Ten year ICON/MESSy-CLaMS simulation climatology (right panels). DJF seasonal mean top and SON bottom.
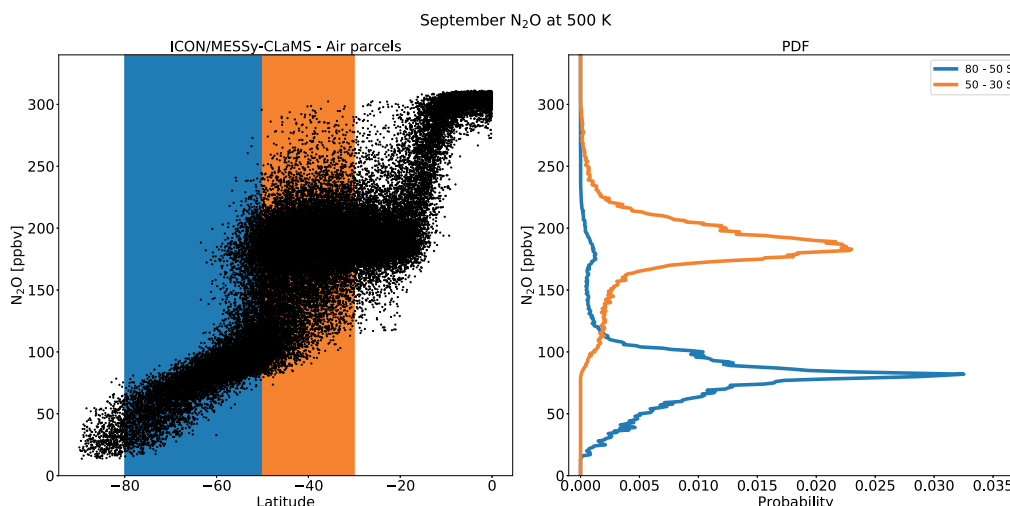

Figure 6: Scatter plot of N_2O mixing ratios of simulated air parcels by ICON/MESSy-CLaMS in September at a potential temperature of 500 K (about 18 km). Latitude bin of 80° S to 50° S is shaded in blue. Latitude bin of 50° S to 30° S is shaded in orange (left panel). Within the latitude bin a PDF is calculated and the probability is shown as a function of the volume mixing ratio (right panel). The colour code indicates the latitude bin of the left panel.

tions, the edge of the polar vortex shows more zonal fluctuations than the simulation, both for northern and southern hemisphere winter (Figure 5).

4.3 Stratospheric transport barriers

We investigate the chemical separation of air masses from a statistical perspective (SPARLING, 2000) using probability distribution functions (PDF) for both, MLS observations and the results of the simulation. Since MLS satellite observations are not uniformly distributed over the hemisphere, but oversample the high latitudes, one has to consider weighting according to the latitudinal area covered by the measurements. Figure 6 shows a schematic how the PDF of two different latitudinal

bands are connected as a scatter plot of data points in a volume mixing ratio versus latitude cross section.

In the left panel of Figure 6 simulated air parcels for September are shown in a scatter plot of volume mixing ratio versus latitude for the southern hemisphere at 500 K (about 18 km). There are two latitudinal bands highlighted with colour shades in the background. One latitudinal band from 30° S to 50° S in orange and one for the latitudinal band of 50° S to 80° S in blue. The corresponding PDFs are shown in the right panel colour coded according to the latitude bands in the left panel. The air masses in the mid-latitude band from 30° S to 50° S contain with the highest probability nitrous oxide with a volume mixing ratio (for an isentropic level of 500 K) of 186 ± 15 ppb. There is a small probability
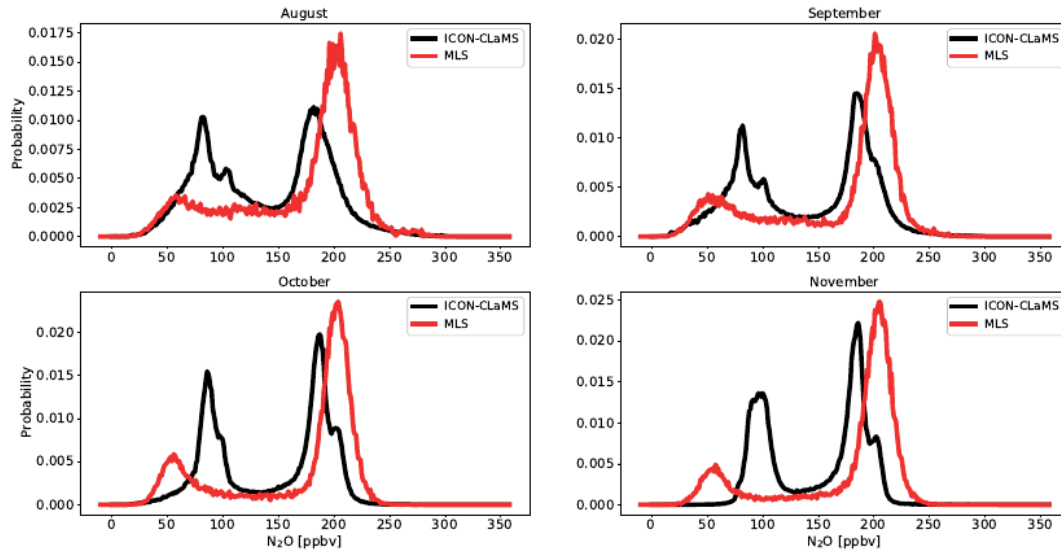
Figure 7: Probability density function (PDF) of N$_2$O mixing ratios in the latitude band 80° S to 30° S at 500 K potential temperature. PDFs of MLS data are marked in red. Simulated ICON/MESSy-CLaMS PDFs are marked in black. The different panels show different months.

for nitrous oxide with a volume mixing ratio in the range of 100 to 150 ppb. The air masses in the latitude band from 50° S to 80° S contain nitrous oxide with a volume mixing ratio of 79 ± 9 ppb with peak probability. The main peaks of the PDFs are distinct in volume mixing ratio. The air masses of both latitudinal bands can be considered distinct in chemical composition and can be considered midlatitude air masses and polar region air masses, respectively. The separation of both PDFs therefore allows the separation of midlatitude from polar air masses to be analysed.

4.4 Antarctic vortex

The PDFs considered in this section contain data from the latitudinal bands, 80° S to 50° S and 50° S to 30° S, combined. Thus, the PDFs of observed (MLS) and simulated N$_2$O volume mixing ratios (August to November) are calculated here in the band from 80° S to 30° S (Figure 7). The single peak structure from the PDFs of two different latitudinal bands discussed previously (Figure 6) are combined (Figure 7) resulting in a double peak structure. Midlatitude and polar vortex air masses can contribute to all volume mixing ratios in the PDF and might broaden the double peak structure. The black lines (Figure 7) denote the PDF from 80° S to 30° S for the simulated air parcels; the red lines denote the observed values for the corresponding months of the year 2005 of the MLS data (Figure 7).

In the ICON/Messy-CLaMS simulated nitrous oxide the separation between the air masses is prominent during all months, where the peak for the midlatitude air mass is shifted to lower volume mixing ratio at around 220 ppb. The simulated peak for the vortex air masses is overestimated. In the mixing ratio range characteristic for mid-latitude air (around 220 ppm of N$_2$O),

the simulated PDF is similar to the observed PDF. However, the peak for the lower volume mixing ratios in polar vortex air masses is overestimated in the simulation (Figure 7).

4.5 Maximum horizontal gradient of nitrous oxide at the edge of the Antarctic vortex

As a measure of the transport barrier at the edge of the Antarctic vortex, the horizontal gradient of nitrous oxide for September at 450 K (~15 km, top), 500 K (~18 km, middle), and 550 K (~20 km, bottom) is shown in Figure 8; both for MLS climatologies as well as for the results of the simulation with ICON/MESSy-CLaMS. (To calculate climatologies and gradients, MLS measurements were used as described in Sec. 2.4 and ICON/MESSy-CLaMS results were interpolated on a regular latitude/longitude grid.) Clearly, nitrous oxide mixing ratios for both, measurements and simulation show a pronounced transport barrier visible as a strong enhancement of the N$_2$O gradient at the edge of the polar vortex. However, on all theta levels in September in the lower stratosphere (450 K, 500 K, and 550 K) the simulation shows a more narrow edge of the vortex (covering a smaller latitude range) than the observations. Further, in the simulation, the transport barrier is located more equatorward, (i.e. the vortex is larger than observed). The observed transport barrier is also more variable than the simulated one.

A similar picture also emerges for the horizontal gradient of nitrous oxide for October and November (not shown, see, SONNABEND, 2024). However, the simulated transport barrier at the edge of the Antarctic vortex at lower altitudes (450 K, 500 K) is weaker than observed.

The transport barrier at the edge of the Antarctic vortex, can be analysed considering specific transects of
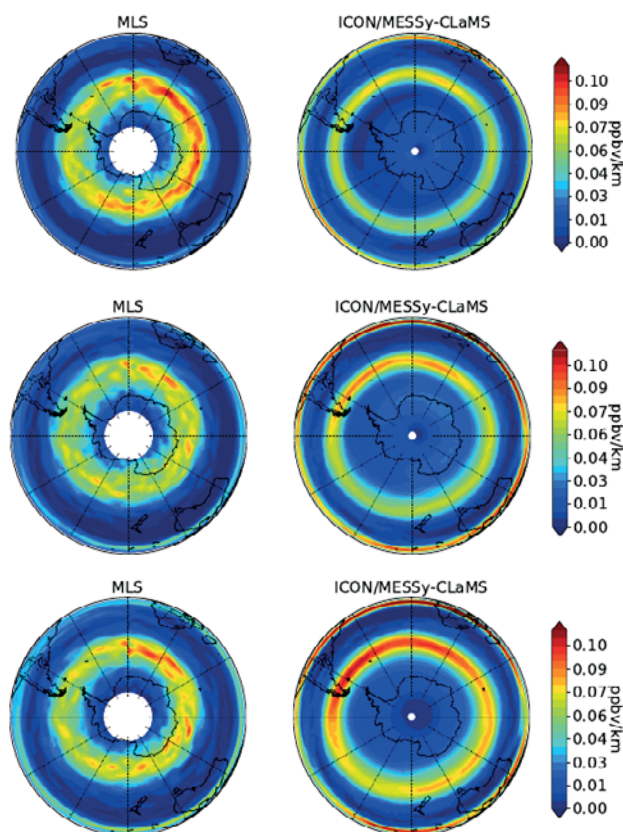
Figure 8: Horizontal N$_2$O gradient in the southern hemisphere in September at 450 K (~15 km, top), 500 K (~18 km, middle) and 550 K (~20 km, bottom). For MLS (left panels), the horizontal N$_2$O gradient is calculated from monthly means on a regular grid (calculated as described in Sec. 2.4) For ICON/MESSy-CLaMS (right panels) the calculation is performed in a similar way (Sec. 2.4). Gradients are calculated from monthly mean 2005–2017 MLS climatologies (left panels) and monthly mean of a ten year (perpetual) simulation of ICON/MESSy-CLaMS (right panels).
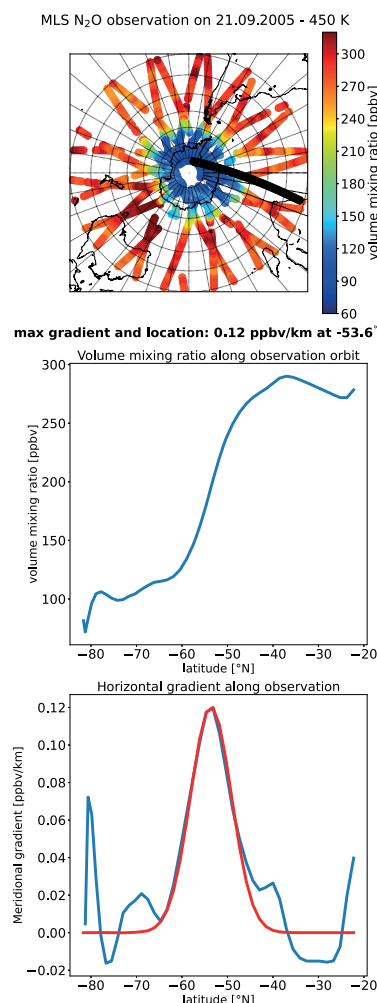

Figure 9: MLS observations of N$_2$O in the southern polar region. The satellite orbit and the corresponding observational locations are accumulated for 24 hours. In the top panel the day 21 September 2005 is shown as an example. Along one orbit trajectory the volume mixing ratio of N$_2$O (middle panel), the latitudinal gradient (bottom panel) and the Gaussian fit to the latitudinal gradient (bottom panel, red line) is shown. The analysed orbit is marked with black dots in the top panel. Whenever the position of the maximum horizontal gradient is outside the interval 70° S to 40° S, the transect was neglected. Furthermore, any transect is removed from the analysis, when two consecutive measurement points are missing.

MLS measurements of N$_2$O mixing ratios following the flight path of the Aura satellite (Figure 9). The Antarctic polar region is transected by MLS 15 times a day. As an example, the accumulated observations on 21 September 2005 are shown in the top panel of Figure 9 for the 450 K isentropic level.

The observed volume mixing ratio along a specific satellite transect (marked with black dots in the top panel) is plotted versus latitude in the middle panel. Furthermore, the gradient along the latitude direction is calculated. Within the range of 70° S to 40° S a Gaussian curve is fitted to the observed gradient. The question, how the maximum observed gradient of N$_2$O in latitudinal direction at the edge of the Antarctic vortex compares with the results of the ICON/CLaMS-MESSy simulation is addressed in Figure 10 below.

Clearly, the changing N$_2$O values across the edge of the Antarctic vortex are visible as a particularly strong horizontal gradient of N$_2$O (with low N$_2$O values inside the vortex). However, MLS satellite observations have a somewhat limited vertical (and horizontal) res-

olution (LIVESEY et al., 2021). Even more pronounced horizontal gradients of N$_2$O are observed in in-situ measurements when entering the Antarctic vortex (IVANOVA et al., 2008).

The values for the maximum horizontal gradient in N$_2$O are calculated as described above (see also Figure 9, bottom), they are accumulated for three days and an average value is calculated. This is done for different isentropic surfaces. The analysis of the maximum gradient determined in this way for the time period June and January on the isentropic surfaces from 450 K to 700 K (~15–26 km) is shown for the MLS observations (Figure 10, left panels) and the ICON/MESSy-CLaMS sim-
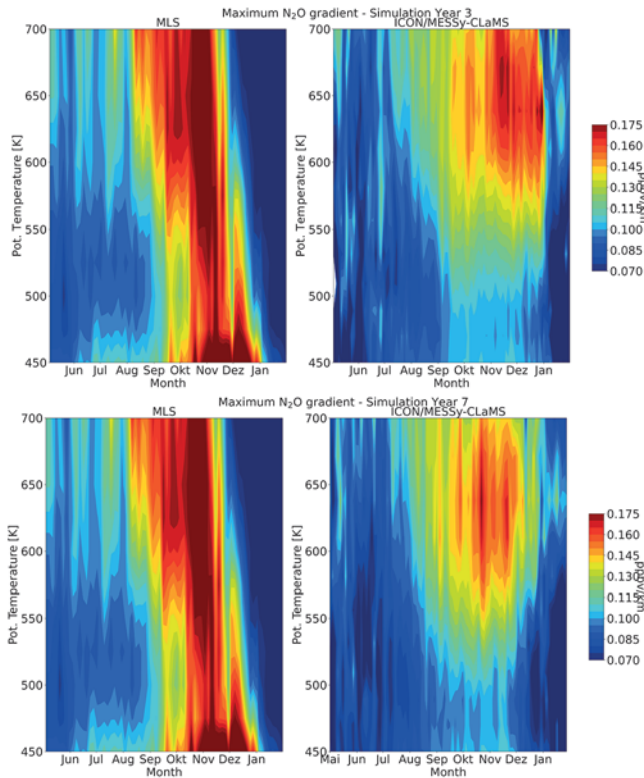
Figure 10: Time series of maximum gradient of nitrous oxide (N_2O) in latitudinal direction in vertical range from 450 K (~15 km) potential temperature up to 700 K (~26 km) at the edge of the Antarctic vortex. The maximum gradient of N_2O is determined for the extratropical southern hemisphere (see Figure 9, bottom right). Top row: MLS 2005 observations (left panel), ICON/MESSy-CLaMS simulation Year 3 (top right panel). Bottom row: MLS 2005 observations (left panel), ICON/MESSy-CLaMS simulation Year 7 (bottom right panel). For MLS (left panels), the horizontal N_2O gradient is calculated along MLS orbits (see Figure 9); for ICON/MESSy-CLaMS (right panels) the calculation is performed in a similar way but for a regular latitude/longitude grid with a 10° spacing in longitude. Data shown in the figure are three-day means.

ulation (Figure 10, right top panel, perpetual year 3; right bottom panel, perpetual year 7). (The years 3 and 7 are selected as examples, see SONNABEND, 2024, for more information.)

There is some variability in the individual years of the time slice run (right column in Figure 10); there is also a certain year-to-year variability in the observations (not shown, see SONNABEND, 2024).

The overall strength of the transport barrier (in mixing ratio per km) is similar for the simulation and the observation, however the simulated transport barrier looses its strength below about 550 K (~20 km) while the observations show that the transport barrier extends down to 450 K (~15 km).

The observed transport barrier gains in strength starting in August (at the top potential temperature levels); it rapidly looses strength at 700 K (~26 km) in late November, while at 450 K (~15 km) there remains a transport barrier until early January (Figure 10, left panels). In contrast, the ICON/MESSy-CLaMS simulation

indicates the existence of a transport barrier until too late in the season (above about 550 K, ~20 km).

Note that there is no discrepancy between the results shown in Figs. 8 and 10; Figure 8 shows September conditions, the strength of the transport barrier (N_2O gradient) increases in the MLS observations in November and October, and moves to lower potential temperature surfaces (SONNABEND, 2024).

5 Discussion

This paper describes the transport of atmospheric constituents and the representation of atmospheric transport barriers in climate models. We argue here that when transport is simulated in the model employing Lagrangian methods, problems caused by numerical diffusion in Eulerian schemes can be reduced (e.g., MCKENNA et al., 2002a; CHARLESWORTH et al., 2023; PLOEGER et al., 2024). However, we also acknowledge that there are limitations. Here we employ ICON in a horizontal resolution of approximately 158 km, corresponding to a 2° × 2° grid. This horizontal resolution may not be be sufficient to accurately resolve small scale features like sharp boundaries of transport barriers (e.g., the jet or the tropopause).

Some discrepancies between the observations and the Lagrangian simulations may be caused by the underlying ICON winds, which include diffusion related to the ICON dynamical core (as the ICON dynamical core is not Lagrangian). The same is true for ERA5, where the underlying model (e.g., section 2.5) is also diffusive to a certain extent. Ideally, one would envisage a dynamical core employing Lagrangian techniques that allow the numerical diffusion of the dynamical core to be better controlled; here progress is difficult as such models are currently not under development.

Further, comparisons of the results of simulations with the ICON/MESSy-CLaMS model with MLS-N_2O observations (Figure 4) also suffer from the uncertainty of MLS measurements, especially at lower altitudes; the MLS uncertainty at ~400 K is 44 % and at ~460 K is 22 %. And the results of the perpetual model simulations for N_2O for 2005 can only be expected to be comparable to, but not *very* close to an observed MLS N_2O climatology for 2005–2017.

In future studies further issues should be explored. First, tests of the transport (e.g., N_2O) in the default Eulerian transport scheme of ICON (REINERT, 2020; REINERT and ZÄNGL, 2021) and comparison with the Lagrangian techniques described here should be performed. Also conducting ensemble simulations would be a way to better characterise the inherent uncertainties of model simulations. Further tests with an increased horizontal resolution (and tests of the sensitivity of the results on the chosen resolution) would be helpful. Finally, results may be improved by employing Lagrangian methods, which work directly on ICON's native triangular grid. Implementing such Lagrangian

Meteorol. Z. (Contrib. Atm. Sci.)
Early Access Article, 2014

J. Sonnabend et al.: Lagrangian transport in ICON

11

methods into the dynamical core or the transport scheme has the potential to reduce numerical diffusion in global models.

6 Conclusions

Horizontal winds and vertical velocities on the ICON grid (where vertical velocities are deduced from diabatic terms calculated in the ICON model) were integrated into a Lagrangian transport simulation based on the CLaMS model. Horizontal winds on the ICON grid were interpolated onto a regular latitude-longitude grid to drive the CLaMS transport. Zonal mean diabatic heating rates (that determine the vertical transport) deduced from ICON temperature tendencies agree reasonably well with ERA5 heating rates. A close correspondence is not expected as the ICON heating rates are deduced from a free running simulation, which is not nudged to observed conditions.

The transport in the ICON/MESSy-CLaMS model is tested through comparison with N_2O measurements by the MLS instrument. The model simulation, consistent with MLS observations, shows a decline of N_2O with altitude, which is caused by chemical loss of N_2O at greater heights in the stratosphere (above a potential temperature of about $500\,K$). Further, upward transport of N_2O in the tropical pipe and diabatic descent over the winter poles is represented in the model simulation.

A focus of the comparisons presented here is on the Antarctic vortex. Clearly both, the observations and the simulation for the Antarctic show the transport barrier at the edge of the vortex (horizontal maps of N_2O mixing ratios). The transport barrier is manifested as a strong enhancement of the latitudinal N_2O gradient. The simulation shows a larger than observed vortex and the transport barrier is less variable in the simulation than in the observations. Both, the simulation and the observations show low N_2O mixing ratios in the Antarctic vortex which are caused by diabatic descent. The strength of the transport barrier in October and November in the MLS observations extends down to $450\,K$ ($\sim15\,km$), while the simulation indicates a substantial reduction of the strength of the transport barrier below about $550\,K$ ($\sim20\,km$).

The transport barrier at the edge of the polar vortex was analysed with the help of PDFs of N_2O mixing ratios with respect to latitude. These PDFs allow polar and mid-latitude airmasses to be clearly distinguished in the simulations as a double peak structure for the period when the polar vortex is present (August–November). The double peak structure is similarly seen in the observations albeit the observed peak in the N_2O PDF is generally higher and shifted somewhat towards higher N_2O mixing ratios than simulated.

Overall there is an agreement regarding the main characteristics in stratospheric transport. The polar vortex (and the associated transport barrier at its edge) is well represented in the simulations, although the simulated polar vortex is larger than observed. Using Lagrangian transport calculations, in general, a good representation of atmospheric transport barriers is possible. We argue that the coupled ICON/MESSy-CLaMS transport scheme allows tracer distributions in the free troposphere and in the stratosphere to be better simulated than by classical Eulerian schemes. In future work, the impact of the spatial resolution in ICON and CLaMS on the results of the simulation will be investigated, comparisons with the default Eulerian transport scheme of ICON will be done and employing Lagrangian methods, which work directly on ICON's native triangular grid, is envisaged.

Appendix 1: GRid AGGregation (GRAGG)

In this study GRid AGGregation (GRAGG) is used to interpolate the ICON variables from the ICON horizontal grid structure to a globally regular longitude-latitude grid (KERN and JÖCKEL, 2016). GRAGG was developed as a diagnostic submodel within the MESSy framework to calculate variables of interest online during the ICON integration time step. The user can define a spatial area by coordinates of longitude and latitude and a grid spacing within this region. The diagnosis within this region allows the amount of input and output (I/O) to be reduced because of two main features of grid aggregation. First, arithmetic operations over ICON native grid cells reduce the amount of grid points in output files. Second,

the I/O operations are reduced to the region of interest defined by the user. After the integration time step, the selected prognostic and diagnostic variables of the base-model are aggregated by GRAGG to the chosen regular longitude-latitude grid on each vertical ICON level. In this work, a global longitude-latitude grid of $2° \times 2°$ is defined. The meteorological information for the CLaMS trajectory calculation is required globally. ICON diagnostic wind components, temperature and pressure, surface pressure, and temperature tendencies (described in Sec. 3.2) are diagnosed on the aggregated grid by an arithmetic average of the native ICON grid points. For the wind field, the zonal and meridional component of the wind field (u and v) diagnosed by ICON from the edge-normal wind vectors onto the respective grid cell centres via radial basis functions, are used. This approach is justified for longitude-latitude target grids with a resolution comparable to ICON's native grid as it is the case here (Sec. 4.1). The error becomes larger for a stronger deviation in resolution of the target and source grid and in regions with larger spatial gradients. After the grid aggregation by GRAGG the meteorological information is accessible for CLaMS input. With the diagnosed meteorological fields, the CLaMS vertical levels are calculated according to the vertical coordinate (Pommrich et al., 2014). Furthermore, the operational call of the GRAGG diagnostics is required during each iteration step, as the updated variables are needed for the CLaMS advection calculation at every time step.

References

Becker, G., J.U. Grooss, D.S. McKenna, R. Müller, 2000: Stratospheric photolysis frequencies: Impact of an improved numerical solution of the radiative transfer equation. – J. Atmos. Chem. **37**, 217–229, DOI: 10.1023/A:1006468926530.

Brinkop, S., P. Jöckel, 2019: Attila 4.0: Lagrangian advective and convective transport of passive tracers within the echam5/messy (2.53.0) chemistry–climate model. – Geosci. Model Dev. **12**, 1991–2008, DOI: 10.5194/gmd-12-1991-2019.

Charlesworth, E., F. Ploeger, T. Birner, R. Baikhadzhaev, M. Abalos, L. Abraham, H. Akiyoshi, S. Bekki, F. Dennison, P. Jöckel, J. Keeble, D. Kinnison, O. Morgenstern, D. Plummer, E. Rozanov, S. Strode, G. Zeng, M. Riese, 2023: Stratospheric water vapor affecting atmospheric circulation. – Nat. Commun. **14**, 3925.

Charlesworth, E.J., A.K. Dugstad, F. Fritsch, P. Jöckel, F. Plöger, 2020: Impact of Lagrangian transport on lower-stratospheric transport time scales in a climate model. – Atmos. Chem. Phys. **20**, 15227–15245, DOI: 10.5194/acp-20-15227-2020.

Clemens, J., B. Vogel, L. Hoffmann, S. Griessbach, N. Thomas, S. Fadnavis, R. Müller, T. Peter, F. Ploeger, 2024: A multi-scenario lagrangian trajectory analysis to identify source regions of the asian tropopause aerosol layer on the indian subcontinent in august 2016. – Atmos. Chem. Phys. **24**, 763–787.

Crutzen, P.J., 1970: The influence of nitrogen oxides on the atmospheric ozone content. – Quart. J.Roy. Meteor. Soc. **96**, 320–325.

Dhomse, S.S., D. Kinnison, M.P. Chipperfield, R.J. Salawitch, I. Cionni, M.I. Hegglin, N.L. Abraham, H. Akiyoshi, A.T. Archibald, E.M. Bednarz, S. Bekki, P. Braesicke, N. Butchart, M. Dameris, M. Deushi, S. Frith, S.C. Hardiman, B. Hassler, L.W. Horowitz, R.M. Hu, P. Jöckel, B. Josse, O. Kirner, S. Kremser, U. Langematz, J. Lewis, M. Marchand, M. Lin, E. Mancini, V. Marécal, M. Michou, O. Morgenstern, F.M. O'Connor, L. Oman, G. Pitari, D.A. Plummer, J.A. Pyle, L.E. Revell, E. Rozanov, R. Schofield, A. Stenke, K. Stone, K. Sudo, S. Tilmes, D. Visioni, Y. Yamashita, G. Zeng, 2018: Estimates of ozone return dates from chemistry-climate model initiative simulations. – Atmos. Chem. Phys. **18**, 8409–8438, DOI: 10.5194/acp-18-8409-2018.

Fadnavis, S., R. Müller, G. Kalita, M. Rowlinson, A. Rap, J.L.F. Li, B. Gasparini, A. Laakso, 2019: The impact of recent changes in asian anthropogenic emissions of SO_2 on sulfate loading in the upper troposphere and lower stratosphere and the associated radiative changes. – Atmos. Chem. Phys. **19**, 9989–10008, DOI: 10.5194/acp-19-9989-2019.

Fueglistaler, S., B. Legras, A. Beljaars, J.J. Morcrette, A. Simmons, A.M. Tompkins, S. Uppapla, 2009: The diabatic heat budget of the upper troposphere and lower/mid stratosphere in ECMWF reanalyses. – Quart. J.Roy. Meteor. Soc. **135**, 21–37, DOI: 10.1002/qj.361.

Giorgetta, M.A., R. Brokopf, T. Crueger, M. Esch, S. Fiedler, J. Helmert, C. Hohenegger, L. Kornblueh, M. Köhler, E. Manzini, T. Mauritsen, C. Nam, T. Raddatz, S. Rast, D. Reinert, M. Sakradzija, H. Schmidt, R. Schneck, R. Schnur, L. Silvers, H. Wan, G. Zängl, B. Stevens, 2018: ICON-A, The Atmosphere Component of the ICON Earth System Model: I. Model Description. – J. Adv. Mod. Earth Sys. **10**, 1613–1637, DOI: 10.1029/2017MS001242.

Grooss, J.U., R. Müller, 2021: Simulation of record arctic stratospheric ozone depletion in 2020. – J. Geophys. Res. **126**, e2020JD033339, DOI: 10.1029/2020JD033339.

Grooss, J.U., I. Engel, S. Borrmann, W. Frey, G. Günther, C.R. Hoyle, R. Kivi, B.P. Luo, S. Molleker, T. Peter, M.C. Pitts, H. Schlager, G. Stiller, H. Vömel, K.A. Walker, R. Müller, 2014: Nitric acid trihydrate nucleation and denitrification in the Arctic stratosphere. – Atmos. Chem. Phys. **14**, 1055–1073, DOI: 10.5194/acp-14-1055-2014.

Hersbach, H., B. Bell, P. Berrisford, S. Hirahara, A. Horànyi, Muñoz J. Sabater, J. Nicolas, C. Peubey, R. Radu, D. Schepers, A. Simmons, C. Soci, S. Abdalla, X. Abellan, G. Balsamo, P. Bechtold, G. Biavati, J. Bidlot, M. Bonavita, G. De Chiara, P. Dahlgren, D. Dee, M. Diamantakis, R. Dragani, J. Flemming, R. Forbes, M. Fuentes, A. Geer, L. Haimberger, S. Healy, R.J. Hogan, E. Hólm, M. Janiskovà, S. Keeley, P. Laloyaux, P. Lopez, C. Lupu, G. Radnoti, P. de Rosnay, I. Rozum, F. Vamborg, S. Villaume, J.N. Thépaut, 2020: The ERA5 global reanalysis. – Quart. J.Roy. Meteor. Soc. **146**, 1999–2049, DOI: 10.1002/qj.3803.

Hoppe, C.M., L. Hoffmann, P. Konopka, J.U. Grooss, F. Ploeger, G. Günther, P. Jöckel, R. Müller, 2014: The implementation of the CLaMS lagrangian transport core into the chemistry climate model EMAC 2.40.1: application on age of air and transport of long-lived trace species. – Geosci. Model Dev. **7**, 2639–2651, DOI: 10.5194/gmd-7-2639-2014.

Hoppe, C.M., F. Ploeger, P. Konopka, R. Müller, 2016: Kinematic and diabatic vertical velocity climatologies from a chemistry climate model. – Atmos. Chem. Phys. **16**, 6223–6239, DOI: 10.5194/acp-16-6223-2016.

Meteorol. Z. (Contrib. Atm. Sci.)
Early Access Article, 2014

J. Sonnabend et al.: Lagrangian transport in ICON

13

IVANOVA, E.V., C.M. VOLK, O. RIEDIGER, H. KLEIN, N.M. SIT-NIKOV, A.E. ULANOVSKII, V.A. YUSHKOV, F. RAVEGNANI, T. MÖBIUS, U. SCHMIDT, 2008: A quasi-lagrangian coordinate system based on high resolution tracer observations: implementation for the Antarctic polar vortex. – Atmos. Chem. Phys. Discuss. **8**, 16123–16173, DOI: 10.5194/acpd-8-16123-2008.

JÖCKEL, P., R. SANDER, A. KERKWEG, H. TOST, J. LELIEVELD, 2005: Technical note: The modular earth submodel system (messy) – a new approach towards Earth system modeling. – Atmos. Chem. Phys. **5**, 433–444.

JÖCKEL, P., H. TOST, A. POZZER, C. BRÜHL, J. BUCHHOLZ, L. GANZEVELD, P. HOOR, A. KERKWEG, M. LAWRENCE, R. SANDER, B. STEIL, G. STILLER, M. TANARHTE, D. TARABORRELLI, J. VAN AARDENNE, J. LELIEVELD, 2006: The atmospheric chemistry general circulation model ECHAM5/MESSy1: consistent simulation of ozone from the surface to the mesosphere. – Atmos. Chem. Phys. **6**, 5067–5104.

JÖCKEL, P., H. TOST, A. POZZER, M. KUNZE, O. KIRNER, C. BRENNINKMEIJER, S. BRINKOP, S.C. DUY, C. DYROFF, J. ECKSTEIN, F. FRANK, H. GARNY, K.D. GOTTSCHALDT, P. GRAF, V. GREWE, A. KERKWEG, B. KERN, S. MATTHES, A. MERTENS, S. MEUL, M. NEUMAIER, M. NÜTZEL, S. OBERLÄNDER-HAYN, R. RUHNKE, T. RUNDE, R. SANDER, D. SCHARFFE, A. ZAHN, 2016: Earth system integrated modelling (escimo) with the modular earth submodel system (messy) version 2.51. – Geosci. Model Dev. **9**, 1153–1200.

JOECKEL, P., A. KERKWEG, A. POZZER, R. SANDER, H. TOST, H. RIEDE, A. BAUMGAERTNER, S. GROMOV, B. KERN, 2010: Development cycle 2 of the Modular Earth Submodel System (MESSy2). – Geosci. Model Dev. **3**, 717–752, DOI: 10.5194/gmd-3-717-2010.

KASAHARA, A., 1974: Various vertical coordinate systems used for numerical weather prediction. – Mon. Wea. Rev. **102**, 509–522.

KERN, B., P. JÖCKEL, 2016: A diagnostic interface for the ICOsahedral non-hydrostatic (ICON) modelling framework based on the modular earth submodel system (MESSy v2.50). – Geosci. Model Dev. **9**, 3639–3654, DOI: 10.5194/gmd-9-3639-2016.

KONOPKA, P., G. GÜNTHER, D.S. MCKENNA, R. MÜLLER, D. OFFERMANN, R. SPANG, M. RIESE, 2005: How homogeneous and isotropic is stratospheric mixing? Comparison of CRISTA-1 observations with transport studies based on the Chemical Lagrangian Model of the Stratosphere (CLaMS). – Quart. J.Roy. Meteor. Soc. **131**, 565–579, DOI: 10.1256/qj.04.47.

KONOPKA, P., G. GÜNTHER, R. MÜLLER, F.H.S. DOS SANTOS, C. SCHILLER, F. RAVEGNANI, A. ULANOVSKY, H. SCHLAGER, C.M. VOLK, S. VICIANI, L.L. PAN, D.S. MCKENNA, M. RIESE, 2007: Contribution of mixing to upward transport across the tropical tropopause layer (TTL). – Atmos. Chem. Phys. **7**, 3285–3308.

KONOPKA, P., M. TAO, F. PLOEGER, D.F. HURST, M.L. SANTEE, J.S. WRIGHT, M. RIESE, 2022: Stratospheric moistening after 2000. – Geophys. Res. Lett. **49**, e2021GL097609, DOI: 10.1029/2021GL097609.

LEUENBERGER, D., M. KOLLER, O. FUHRER, C. SCHÄR, 2010: A generalization of the SLEVE vertical coordinate. – Mon. Wea. Rev. **138**, 3683–3689.

LIVESEY, N.J., W.G. READ, L. FROIDEVAUX, A. LAMBERT, M.L. SANTEE, M.J. SCHWARTZ, L.F. MILLÁN, R.F. JARNOT, P.A. WAGNER, D.F. HURST, K.A. WALKER, P.E. SHEESE, G.E. NEDOLUHA, 2021: Investigation and amelioration of long-term instrumental drifts in water vapor and nitrous oxide measurements from the Aura Microwave Limb Sounder (MLS) and their implications for studies of variability and trends. – Atmos. Chem. Phys. **21**, 15409–15430, DOI: 10.5194/acp-21-15409-2021.

MCKENNA, D.S., P. KONOPKA, J.U. GROOSS, G. GÜNTHER, R. MÜLLER, R. SPANG, D. OFFERMANN, Y. ORSOLINI, 2002a: A new Chemical Lagrangian Model of the Stratosphere (CLaMS): 1. Formulation of advection and mixing. – J. Geophys. Res. **107**, 4309, DOI: 10.1029/2000JD000114.

MCKENNA, D.S., J.U. GROOSS, G. GÜNTHER, P. KONOPKA, R. MÜLLER, G. CARVER, Y. SASANO, 2002b: A new Chemical Lagrangian Model of the Stratosphere (CLaMS): 2. Formulation of chemistry scheme and initialization. – J. Geophys. Res. **107**, 4256, DOI: 10.1029/2000JD000113.

MILLS, M., O. TOON, R. TURCO, D. KINNISON, R. GARCIA, 2008: Massive global ozone loss predicted following regional nuclear conflict. – Proc. Natl. Acad. Sci. **105**, 5307–5312.

MÜLLER, R., 2021: The impact of the rise in atmospheric nitrous oxide on stratospheric ozone. – Ambio **50**, 42–46, DOI: 10.1007/s13280-020-01428-3.

PLOEGER, F., P. KONOPKA, G. GÜNTHER, J.U. GROOSS, R. MÜLLER, 2010: Impact of the vertical velocity scheme on modeling transport across the tropical tropopause layer. – J. Geophys. Res. **115**, D03301, DOI: 10.1029/2009JD012023.

PLOEGER, F., T. BIRNER, E. CHARLESWORTH, P. KONOPKA, R. MÜLLER, 2024: Moist bias in the Pacific upper troposphere and lower stratosphere (UTLS) in climate models affects regional circulation patterns. – Atmos. Chem. Phys. **24** 2033–2043, DOI: 10.5194/acp-24-2033-2024.

POMMRICH, R., R. MÜLLER, J.U. GROOSS, P. KONOPKA, F. PLOEGER, B. VOGEL, M. TAO, C.M. HOPPE, G. GÜNTHER, N. SPELTEN, L. HOFFMANN, H.C. PUMPHREY, S. VICIANI, F. D'AMATO, C.M. VOLK, P. HOOR, H. SCHLAGER, M. RIESE, 2014: Tropical troposphere to stratosphere transport of carbon monoxide and long-lived trace species in the Chemical Lagrangian Model of the Stratosphere (CLaMS). – Geosci. Model Dev. **7**, 2895–2916, DOI: 10.5194/gmd-7-2895-2014.

PORTMANN, R.W., J.S. DANIEL, A.R. RAVISHANKARA, 2012: Stratospheric ozone depletion due to nitrous oxide: influences of other gases. – Phil. Trans. R. Soc. B **367**, 1256–1264, DOI: 10.1098/rstb.2011.0377.

POSHYVAILO-STRUBE, L., R. MÜLLER, S. FUEGLISTALER, M.I. HEGGLIN, J.C. LAUBE, C.M. VOLK, F. PLOEGER, 2022: How can Brewer–Dobson circulation trends be estimated from changes in stratospheric water vapour and methane? – Atmos. Chem. Phys. **22**, 9895–9914, DOI: 10.5194/acp-22-9895-2022.

RAVISHANKARA, A.R., J.S. DANIEL, R.W. PORTMANN, 2009: Nitrous oxide (N_2O): The dominant ozone-depleting substance emitted in the 21st century. – Science **326**, 123–125, DOI: 10.1126/science.1176985.

REINERT, D., 2020: The tracer transport module part I: A mass consistent finite volume approach with fractional steps. Technical Report 5, DWD, Reports on ICON, DOI: 10.5676/DWD_pub/nwv/icon_005.

REINERT, D., G. ZÄNGL, 2021: The tracer transport module part II: Description and validation of the vertical transport operator. Technical Report 7, DWD, Reports on ICON, DOI: 10.5676/DWD_pub/nwv/icon_007.

ROBOCK, A., L. XIA, C.S. HARRISON, J. COUPE, O.B. TOON, C.G. BARDEEN, 2023: Opinion: How fear of nuclear winter has helped save the world, so far. – Atmos. Chem. Phys. **23**, 6691–6701, DOI: 10.5194/acp-23-6691-2023.

ROSANKA, S., R. SANDER, B. FRANCO, C. WESPES, A.. WAHNER, D. TARABORRELLI, 2021: Oxidation of low-molecular-weight organic compounds in cloud droplets: global impact on tropospheric oxidants. – Atmos. Chem. Phys. **21**, 9909–9930, DOI: 10.5194/acp-21-9909-2021.

Ruiz, D.J., M.J. Prather, 2022: From the middle stratosphere to the surface, using nitrous oxide to constrain the stratosphere–troposphere exchange of ozone. – Atmos. Chem. Phys. **22**, 2079–2093, DOI: 10.5194/acp-22-2079-2022.

Sander, R., A. Baumgaertner, D. Cabrera-Perez, F. Frank, S. Gromov, J.U. Grooss, H. Harder, V. Huijnen, P. Jöckel, V.A. Karydis, K.E. Niemeyer, A. Pozzer, H. Riede, M.G. Schultz, D. Taraborrelli, S. Tauer, 2019: The community atmospheric chemistry box model CAABA/MECCA-4.0. – Geosci. Model Dev. **12**, 1365–1385, DOI: 10.5194/gmd-12-1365-2019.

Sonnabend, J., 2024: Horizontal gradients of nitrous oxide in Lagrangian chemical transport induced by ICON-NWP model. – Ph.D. thesis, https://elekpub.bib.uni-wuppertal.de/ubwhs/content/titleinfo/7547100, DOI: 10.25926/BUW/0-314.

Sparling, L.C., 2000: Statistical perspectives on stratospheric transport. – Rev. Geophys. **38**, 417–436.

Sutton, R.T., H. Maclean, R. Swinbank, A. O'Neill, F.W. Taylor, 1994: High-resolution stratospheric tracer fields estimated from satellite observations using Lagrangian trajectory calculations. – J. Atmos. Sci. **51**, 2995–3005.

Taylor, K.E., D. Williamson, F. Zwiers, 2000: The sea surface temperature and sea ice concentration boundary conditions for AMIP II simulations. PCMDI Report 60. Program for Climate Model Diagnosis and Intercomparison. – Technical report, Lawrence Livermore National Laboratory, https://pcmdi.llnl.gov/report/pdf/60.pdf.

Tilmes, S., J.H. Richter, B. Kravitz, D.G. MacMartin, A.S. Glanville, D. Visioni, D.E. Kinnison, R. Müller, 2021: Sensitivity of total column ozone to stratospheric sulfur injection strategies. – Geophys. Res. Lett. **48**, e2021GL094058, DOI: 10.1029/2021GL094058.

Visioni, D., B. Kravitz, A. Robock, S. Tilmes, J. Haywood, O. Boucher, M. Lawrence, P. Irvine, U. Niemeier, L. Xia, G. Chiodo, C. Lennard, S. Watanabe, J.C. Moore, H. Muri, 2023: Opinion: The scientific and community-building roles of the geoengineering model intercomparison project (geomip) – past, present, and future. – Atmos. Chem. Phys. **23**, 5149–5176, DOI: 10.5194/acp-23-5149-2023.

Vogel, B., R. Müller, G. Günther, R. Spang, S. Hanumanthu, D. Li, M. Riese, G.P. Stiller, 2019: Lagrangian simulations of the transport of young air masses to the top of the Asian monsoon anticyclone and into the tropical pipe. – Atmos. Chem. Phys. **19**, 6007–6034, DOI: 10.5194/acp-19-6007-2019.

Vogel, B., C.M. Volk, J. Wintel, V. Lauther, J. Clemens, J.U. Grooss, G. Günther, L. Hoffmann, J.C. Laube, R. Müller, F. Ploeger, F. Stroh, 2024: Evaluation of vertical transport in ERA5 and ERA-interim reanalysis using high-altitude aircraft measurements in the Asian summer monsoon 2017. – Atmos. Chem. Phys. **24**, 317–343.

Waters, J.W., L. Froidevaux, R.S. Harwood, R.F. Jarnot, H.M. Pickett, W.G. Read, P.H. Siegel, R.E. Cofield, M.J. Filipiak, D.A. Flower, J.R. Holden, G.K. Lau, N.J. Livesey, G.L. Manney, H.C. Pumphrey, M.L. Santee, D.L. Wu, D.T. Cuddy, R.R. Lay, M.S. Loo, V.S. Perun, M.J. Schwartz, P.C. Stek, R.P. Thurstans, M.A. Boyles, S. Chandra, M.C. Chavez, G.S. Chen, B.V. Chudasama, R. Dodge, R.A. Fuller, M.A. Girard, J.H. Jiang, Y. Jiang, B.W. Knosp, R.C. LaBelle, J.C. Lam, K.A. Lee, D. Miller, J.E. Oswald, N.C. Patel, D.M. Pukala, O. Quintero, D.M. Scaff, W.V. Snyder, M.C. Tope, P.A. Wagner, M.J. Walch, 2006: The Earth Observing System Microwave Limb Sounder (EOS MLS) on the Aura satellite. – IEEE Trans. Geosci. Remote Sens. **44**, 1106–1121.

Zängl, G., D. Reinert, P. Rípodas, M. Baldauf, 2015: The ICON (ICOsahedral Non-hydrostatic) modelling framework of DWD and MPI-M: Description of the non-hydrostatic dynamical core. – Quart. J.Roy. Meteor. Soc. **141**, 563 – 579, DOI: 10.1002/qj.2378.

Zängl, G., D. Reinert, F. Prill, 2022: Grid refinement in ICON v2.6.4. – Geosci. Model Dev. **15**, 7153–7176, DOI: 10.5194/gmd-15-7153-2022.